RSC Advances

PAPER

View Article Online
View Journal | View Issue

Cite this: RSC Adv., 2025, 15, 48795

SiC coated, CNT nanowire reinforced copper composite: preparation, microstructure and properties

Pham Van Trinh, *[ab] Nguyen Binh An,[a] Tran Van Hau, [a] Do Tuan,[a] Nguyen Van Tu,[a] Nguyen Thi Huyen,[a] Tran Bao Trung, [a] Nguyen Van Hao, [c] Nguyen Van Kha,[d] Phan Ngoc Minh[b] and Doan Dinh Phuong[a]

Received 13th August 2025
Accepted 4th December 2025

DOI: 10.1039/d5ra05976c

rsc.li/rsc-advances

Copper matrix composites are engineering materials widely used in electrical and electronic applications. Therefore, enhancing their mechanical, electrical and thermal properties is essential. In this work, some results on the preparation of silicon carbide coated carbon nanotube nanowire (SiC@CNT NWs) reinforced copper (Cu) matrix composites were presented. SiC@CNT NWs prepared using a chemical vapor deposition method were mixed with Cu powder and then consolidated by spark plasma sintering to obtain SiC@CNTNW/Cu composites. The effects of SiC@CNT NW content on the microstructure, mechanical properties, tribological behavior, electrical and thermal properties were examined. Incorporation of 3 vol% SiC@CNT NWs enhanced hardness and ultimate tensile strength by 71% and 64%, respectively, while reducing the coefficient of friction (COF) by 40% and specific wear rate by 53%. These improvements are attributed to the SiC@CNT structure, which offers superior reinforcement efficiency. The coefficient of thermal expansion decreased with increasing nanowire fraction, consistent with the inherently lower CTE of SiC@CNT NWs. Based on Turner's model, the CTE and Young's modulus of the nanowires were estimated at $1.8 \times 10^{-6}\ \mathrm{K}^{-1}$ and 680 GPa, respectively.

1. Introduction

Metal matrix composites (MMCs) are defined as materials composed of two distinct phases, consisting of a metallic matrix and reinforcing agents.[1,2] Optimizing both phases is essential for achieving properties superior to those of the original metal.[3] Among MMCs, copper-based composites are among the earliest developed and remain some of the most extensively studied.[4–7] Cu matrix composites, first developed in the late 1960s, are now widely used in electrical contacts, heat sinks, electronic packaging, and fuel cell electrodes due to their excellent electrical/thermal conductivity, corrosion and wear resistance, and low thermal expansion. Studies also show that adding particulate reinforcements effectively enhances their wear resistance and high-temperature mechanical properties while maintaining the intrinsic electrical and thermal conductivities.[4,8–12] Common reinforcement materials such as Al_2O_3, SiC, TiC, or their hybrid combinations have exhibited superior performance compared to conventional copper alloys.[13–18] Among them, Cu matrix composites reinforced with silicon carbide particles (SiCp) have attracted particular interest due to the high thermal conductivity, high melting point, good mechanical properties (*e.g.*, hardness and wear resistance), and low production cost of SiC.[19,20] These composites have demonstrated promising potential for diverse industrial applications. Câmara *et al.* investigated the influence of SiC content on the microstructure and mechanical behavior of Cu–SiC composites and reported that high-energy ball milling produced severely deformed Cu particles with irregular lamellar structures.[21] Efe *et al.* further showed that increasing SiC content and adjusting sintering temperature promoted a uniform particle distribution, enhanced hardness, but reduced electrical conductivity.[22] Akbarpour *et al.* demonstrated that adding 4 vol% nano-SiC, consolidated by spark plasma sintering (SPS), significantly improved wear resistance and lowered the friction coefficient compared to pure Cu.[23–26] Likewise, Tjong and Lau found that incorporating 20 vol% SiC *via* hot isostatic pressing (HIP) markedly increased wear resistance by suppressing subsurface deformation.[27] Despite these improvements, many SiC–Cu composites still exhibit limited mechanical performance, largely due to weak interfacial bonding between SiC and Cu.[28] Overall, SiC reinforcement clearly enhances the mechanical and physical properties of Cu-based composites, but further advances—particularly the development of nanoscale SiC

---

[a] *Institute of Materials Science, Vietnam Academy of Science and Technology, 18 Hoang Quoc Viet Str., Nghia Do Ward, Hanoi, Vietnam. E-mail: trinhpv@ims.vast.vn*
[b] *Graduate University of Science and Technology, Vietnam Academy of Science and Technology, 18 Hoang Quoc Viet Str., Nghia Do Ward, Hanoi, Vietnam*
[c] *Thai Nguyen University of Sciences, Tan Thinh Ward, Thai Nguyen, Vietnam*
[d] *Institute of Physics, Vietnam Academy of Science and Technology, 10 Dao Tan Str., Giang Vo Ward, Hanoi, Vietnam*

reinforcements with superior characteristics—are needed to achieve high-performance SiC–Cu systems for demanding electrical and electronic applications. Carbon nanotubes (CNTs) have attracted extensive interest as one-dimensional reinforcements in MMCs due to their exceptional tensile strength and structural stability.[29] However, their reinforcing efficiency is limited by the need for long effective load-transfer lengths, low densification, poor high-temperature stability, and weak interfacial bonding with copper, which restricts CNT loading in CNT/Cu composites.[30,31] SiC nanowires have recently emerged as promising alternatives, offering high mechanical strength, excellent thermal conductivity, and tunable electronic properties.[32–35] They have been successfully incorporated into polymer and ceramic matrices, where increasing nanowire content improved wear resistance, albeit at the cost of reduced densification.[36–40]

Recent advancements in the nanoengineering of one-dimensional (1D) nanotubes have enabled the construction of 1D heterostructures—particularly core–shell configurations—that exhibit multifunctional properties surpassing those of their single-component analogues. Coaxial nanotubes can be synthesized by coating a secondary phase onto the surface of pre-formed nanotubes, thereby preserving the intrinsic 1D morphology along the axial direction of the original template. Among various candidates, carbon nanotubes (CNTs) are widely recognized as optimal scaffolds for the fabrication of 1D nanostructures due to their exceptional structural robustness and well-defined geometry. The use of CNTs as templates facilitates spatially confined growth, resulting in heterostructures with geometrical parameters—such as diameter, length, and alignment—closely mirroring those of the CNTs. As a result, considerable attention has been directed toward the template-assisted synthesis of coaxial nanostructures, especially those employing CNTs. Several research groups have successfully fabricated SiC coated CNT (SiC@CNT) nanowires.[41–44] This achievement opens a promising research direction for the use of SiC@CNT nanowire as a novel reinforcement in metal matrix composites. Our previous study demonstrated that aluminum matrix composites reinforced with SiC@CNT nanowires exhibited significantly enhanced mechanical strength and wear resistance.[41] Despite these advancements, the influence of SiC@CNT nanowire on the mechanical and tribological performance of other metal matrix composites (MMCs) remains largely unexplored.

Thus, in this work, we prepared Cu composites reinforced with SiC@CNT nanowires by powder metallurgy method. SiC@CNT nanowires were prepared by the chemical vapor deposition method and used as reinforcement for Cu composite. The effects of nanowire contents on microstructure, mechanical, wear behavior and thermal expansion of the composites have been investigated and discussed.

2. Experimental procedure

2.1. Materials

Lab-synthesized MWCNTs (average diameter: 20 nm; length: 10 μm), Si powder (15.5 μm), and SiO_2 powder (200 nm) obtained from Sigma-Aldrich Co., Ltd were employed for the synthesis of SiC@CNT nanowires. Copper powder (average diameter: 18.5 μm, Kojundo Chemical Laboratory Co., Ltd) served as the matrix material.

2.2. Fabrication of SiC@CNT NW/Cu composites

The fabrication process of SiC@CNT NW/Cu composites is illustrated in Fig. 1a. SiC@CNT NW reinforcement was prepared using the reported process in our previous work.[41] MWCNTs were functionalized with carboxyl groups (–COOH) *via* acid oxidation in a mixed solution of H_2SO_4 and HNO_3 (3 : 1, v/v) at 70 °C for 5 h.[45] The resulting solution was filtered, washed, and redispersed in distilled water, followed by tip sonication for 30 min to obtain a stable CNT suspension. The prepared CNT–COOH was dispersed in $Fe(NO_3)_3$ solution (1 M) for 30 min under magnetic stirring, followed by filtering and drying at 180 °C in vacuum for 24 h to obtain Fe-coated CNT powder. Amounts of Si and SiO_2 (1 : 1) powder were mixed with Fe-coated CNT powder by tip sonication to obtain the catalytic material. The prepared catalytic material was treated at a temperature of 1400 °C for 2 h under Ar atmosphere to prepare SiC@CNT NWs. A designed Cu powder was added and mixed with SiC@CNT NWs in ethanol using a pulse ultrasonic wave of 5 s on/5 s off. Ultrasonication was maintained for 30 min, after which the vessel containing the SiC@CNT NW/Cu suspension was immediately immersed in liquid N_2 for 3 min and subsequently freeze-dried at −68 °C for 48 h under primary vacuum (14 mTorr). The obtained powders were then treated at 280 °C for 60 min in H_2 environment for removing the oxidation phase to obtain SiC@CNT NW/Cu composite powders. The composite powders were consolidated into cylindrical compacts (20 mm in diameter and 4 mm in height) by spark plasma sintering (SPS, Dr Sinter Lab Series) at 700 °C for 5 min in vacuum under a pressure of 50 MPa. For comparison, pure Cu compacts without SiC@CNT NWs were prepared under identical conditions. The prepared samples are noted as S0, S1, S2 and S3 corresponding to pure Cu and composites containing 1 vol%, 2 vol% and 3 vol% SiC@CNT NWs, respectively. The details of the compositions of the sintered composites are listed in Table 1.

2.3. Characterization and testing

The microstructures of the composites were examined using an optical microscope (Axiovert 40 MAT, Germany), a scanning electron microscope (SEM, Hitachi S4800, Japan), and electron backscatter diffraction (EBSD, JEOL JSM-6500F). Phase composition was determined by X-ray diffraction (XRD, Bruker D8 Advance diffractometer). The experimental density of the sintered composites was measured using the Archimedes method, while the theoretical density was calculated using 3.21 and 8.96 g cm^{-3} for SiC and Cu, respectively. Tensile tests were conducted on dog bone-shaped specimens (gauge length: 6 mm; width: 1.7 mm) according to the ASTM E8M standard using a universal testing machine (INSTRON 8848 micro-tester) at a crosshead speed of 0.2 mm min^{-1} at room temperature. Tribological performance was evaluated using a pin-on-disk

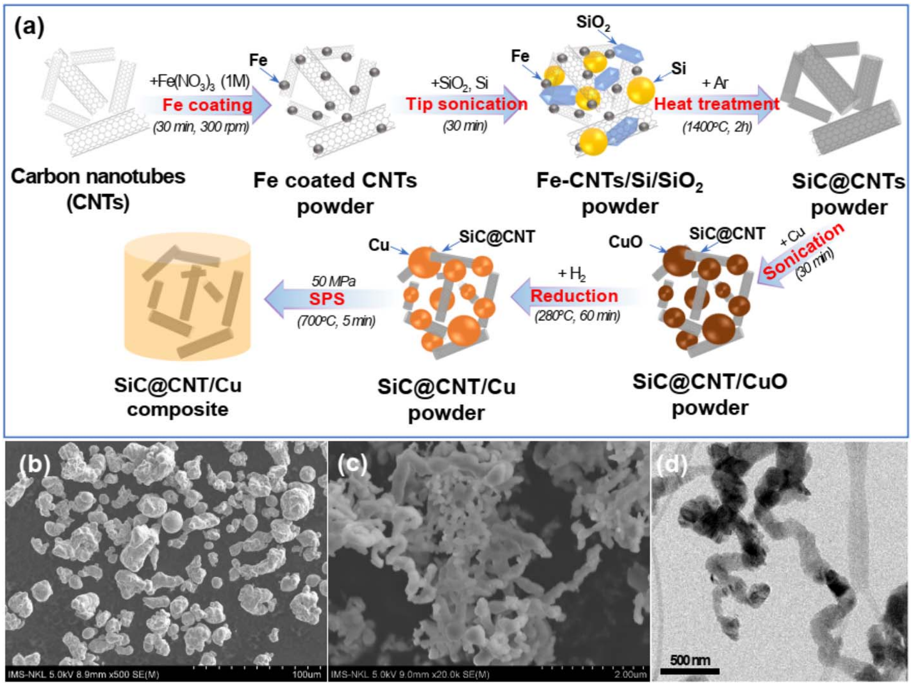

Fig. 1 (a) Preparation process of SiC@CNT NW/Cu composites, (b) SEM image of Cu powder and (c and d) SEM and TEM images of SiC@CNT NW powder.

tribometer (TRB3, Anton Paar) under a 1 N normal load, 100 m sliding distance, and 10 cm s^{-1} linear speed. The electrical conductivity of the samples was determined at room temperature using a four-point probe apparatus (CMT-SR1000N, Advanced Instrument Technology). Thermal conductivity was evaluated by employing the laser flash technique with an LFA 457 instrument (NETZSCH, Germany). The coefficient of thermal expansion (CTE) was measured between 50 and 250 °C using a DIL 402 PC dilatometer. Hardness, tensile strength, and wear resistance values represent the average of five independent measurements for each sample to ensure statistical reliability.

3. Results and discussion

3.1. Microstructure

Fig. 1b and c shows SEM and TEM images of SiC@CNT nanowires. As can be seen, the diameter of SiC@CN nanowires was estimated to be about 100–200 nm. The surface of a coaxial nanocable is not smooth and homogeneous. This can be due to the priority growth point of SiC on the surface of CNTs. Fig. 2 presents the SEM image of the SiC@CNT NW/Cu composite powder containing different SiC@CNT NW contents. As shown in the figure, it is indicated that increasing the SiC@CNT NW contents leads to a higher observed density of these reinforcements within the composite powders. The microstructural analysis indicates that the SiC@CNT NWs are individually dispersed on the surfaces of the Cu particles. This uniform dispersion is important issue because it promotes better interfacial contact between the reinforcement and the matrix, which can enhance load transfer efficiency and improve the overall mechanical properties of the composites. Moreover, preparation process successfully prevents the formation of particle clusters. These observations provide strong evidence that the employed mixing methods are effective in achieving a homogeneous distribution of SiC@CNT NWs. The observation is consistent with previous studies that have employed similar approaches for dispersing CNTs in metal matrices.[46–48] The uniform dispersion of the reinforcement is expected to contribute positively to the performance of the prepared composites.

Table 1 Composition, relative density, hardness, yield strength (σ_{YS}), ultimate tensile strength (σ_{UTS}) and elongation of the SiC@CNT NW/Cu composites

Sample	SiC@CNT content (vol%)	Elastic modulus (GPa)	Yield strength (MPa)	Ultimate tensile strength (MPa)	Elongation (%)
S0	0	101.3	192.7	225.8	16.2
S1	1	108.6	230.1	262.4	10.8
S2	2	110.8	290.5	306.8	6.2
S3	3	124.2	360.1	371.7	1.9

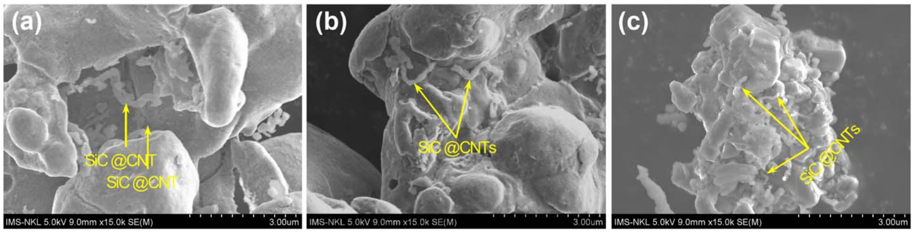

Fig. 2 SEM images of SiC@CNT/Cu composite powder containing different SiC@CNT NW contents (a) 1 vol%, (b) 2 vol% and (c) 3 vol%.

Fig. 3 presents the fracture surface morphologies of the prepared samples. For sample S0, the observed surface exhibits numerous dimples with relatively uniform size and significant depth, and the inner walls of the pits are relatively smooth. These features suggest that the S0 possesses good plastic deformation capability. In contrast, the composite samples S1, S2, and S3 display dimples with non-uniform sizes and depths. Notably, SiC@CNT NWs are observed to be evenly distributed both within the dimples and along their walls. This may result from the strong interfacial bonding between the SiC@CNT NWs and the Cu matrix, which allows the nanowires to remain embedded on the dimples surfaces during deformation. The interfacial bonding between the reinforcement and the Cu matrix may be associated with structural changes at the interfacial layer, contributing to improved mechanical stability and influencing the overall deformation behavior of the composites. Thus, the local formation remains a possibility, and detailed HRTEM analysis in future studies are expected to provide valuable insights into that matter. According to Zhang *et al.*, the enhancement of the interfacial bond strength between reinforcements and metal matrix may be due to a small amount of chemical reaction at the interface.[49] The enhancement will help load transfer from the matrix to nanowires and thus lead to the fracture of nanowires. Moreover, the pull-out and bridging of nanowires could inhibit the propagation of cracks on the submicron scale. As a result, the mechanical properties of Cu composite reinforced by SiC@CNTs were significantly improved.

Fig. 4 illustrates the grain size and its distribution for samples S0, S1, S2, and S3 after sintering. The average grain sizes of the Cu matrix in S0, S1, S2, and S3 were measured to be 1.35, 1.28, 1.17, and 1.08 μm, respectively. The results indicate that increasing the SiC@CNT NW content leads to a progressive reduction in Cu grain size. This refinement is likely due to the presence of SiC@CNT NWs within the Cu matrix, which act as effective barriers to grain growth during sintering.

3.2. XRD analysis

Fig. 5a presents the XRD patterns of the prepared samples. The typical peaks of Cu were identified in all the prepared samples, whereas the typical peaks of SiC were distinctly observed only in sample S3, which contains 3 vol% SiC. In addition, the typical peak of CNT at $2\theta = 26.7°$ was also detected in sample S3. For composites containing lower SiC@CNT NW contents, the typical peaks of SiC and CNT were not observed, which may be attributed to their concentrations being below the detection limit of XRD. Fig. 5b shows the relationship between micro-strain (ε) and crystalline-size (d_c) of the composites calculated by using the Williamson–Hall method from the XRD peak broadening (β_{hkl}) given by:[50,51]

$$\beta_{hkl}\cos\theta = \frac{0.94\lambda}{d_c} + 4\varepsilon\sin\theta \tag{1}$$

where λ is the wavelength of Cu Kα radiation. The values of ε and d_c were estimated from the slope and intercept obtained by plotting and linearly fitting the relationship between $\beta\cos\theta$ and $\sin\theta$. The dislocation density (ρ) was calculated using the following eqn (2):[51]

$$\rho = \frac{2\sqrt{3}\varepsilon}{d_c b} \tag{2}$$

The ρ values were calculated using eqn (2) to be 2.91×10^{14}, 4.26×10^{14}, 4.84×10^{14} and 5.05×10^{14} m^{-2} for the S0, S1, S2 and S3. Thus, it can be seen that increasing the SiC@CNT NW contents leads to a significant increase in the dislocation density. The enhancement in the dislocation density contributes to the improvement of the mechanical properties of the prepared composites.

3.3. Mechanical properties

The relative densities of the prepared samples were calculated to be 99.1%, 98.8%, 98.1 and 97.9% corresponding to S0, S1, S2 and S3, respectively. The obtained results demonstrated that SPS could be used to consolidate the SiC@CNT NW/Cu composites. Fig. 6a shows the hardness of the prepared samples. The measured hardness values were determined to be 52.3, 65.5, 76.3 and 89.5 HV for S0, S1, S2 and S3, respectively. The hardness of S3 is approximately 71% higher than that of S0. The stress–strain curves are shown in Fig. 6b, while the detailed mechanical properties are summarized in Table 1. Both the elastic modulus, yield strength, and ultimate tensile strength increased with the rising content of SiC@CNT nanowires. Notably, the σ_{UTS} of S3 reached ~371.7 MPa, nearly 64% greater than that of S0 (~225.8 MPa). The σ_{YS} of S2 exceeded those of S0, S1, and S3. These results confirm that the incorporation of SiC@CNT nanowires plays a key role in enhancing the hardness and strength of the composites.

Yield strength is commonly employed to evaluate the strengthening behavior of composites. The strengthening efficiency (R) is defined by the following eqn (3):

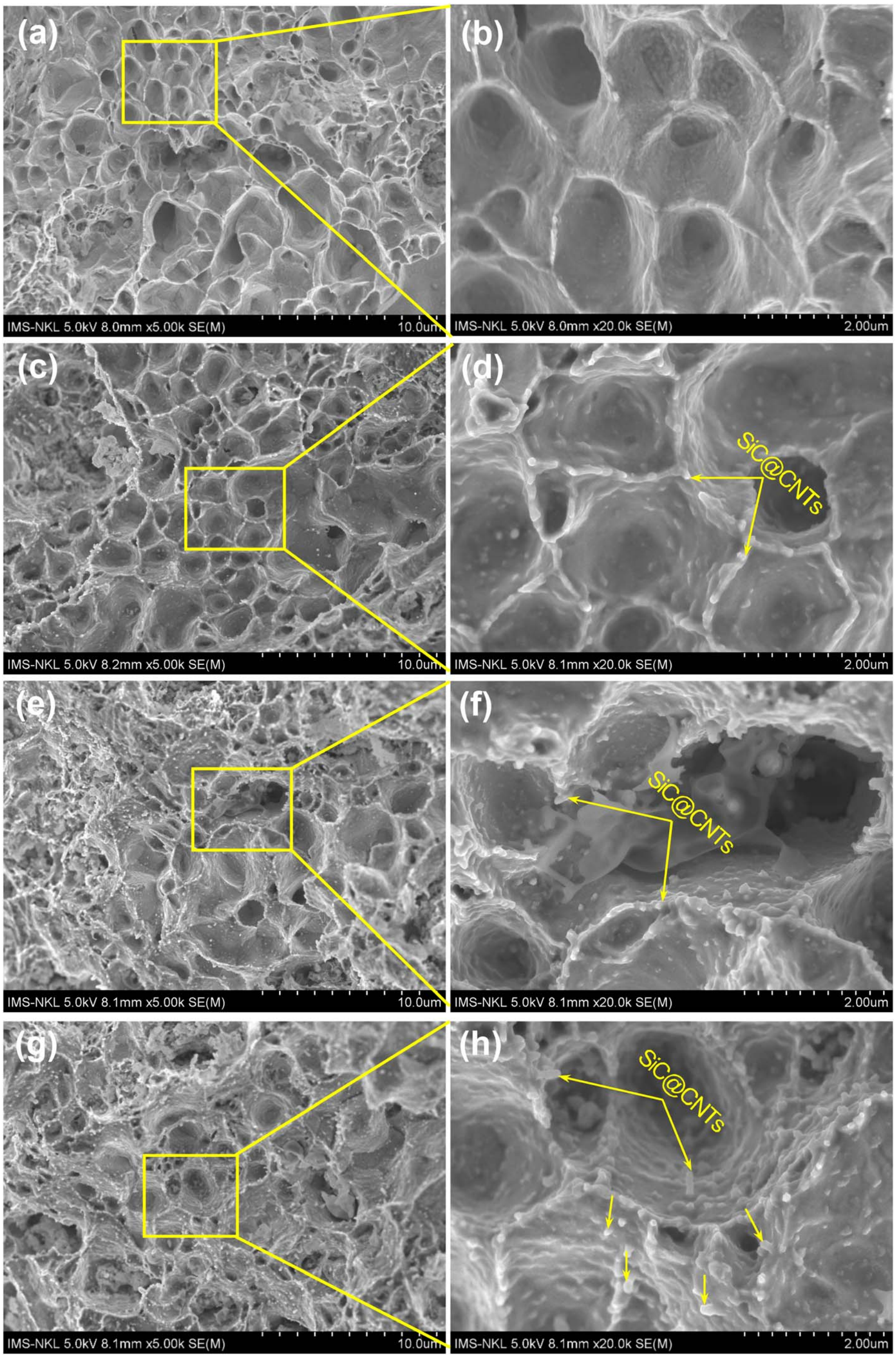

Fig. 3 Fracture surface of (a and b) S0, (c and d) S1, (e and f) S2 and (g and h) composite S3.

$$R = \frac{\sigma_c - \sigma_m}{\sigma_m \times V_f} \tag{3}$$

where σ_c and σ_m denote the yield strength of the composites and pure Cu, respectively, and V_f represents the volume fraction of the reinforcements. The value of R is strongly influenced by the aspect ratio of the reinforcements and the interfacial bonding characteristics between the reinforcement and the matrix. The relationship between strengthening efficiency and the yield strength of Cu composites reinforced with SiC-type reinforcements has been extensively discussed in previous studies.[52–55] The strengthening behavior of SiC-type reinforcements in Cu matrix composites is influenced by both the preparation method and the aspect ratio of the reinforcements. In this study, the strengthening efficiency (R) was calculated to be 28.9, indicating that SiC@CNT NWs enhance the mechanical properties of the composites by combining the exceptional mechanical characteristics of both CNTs and SiC within the composite system.

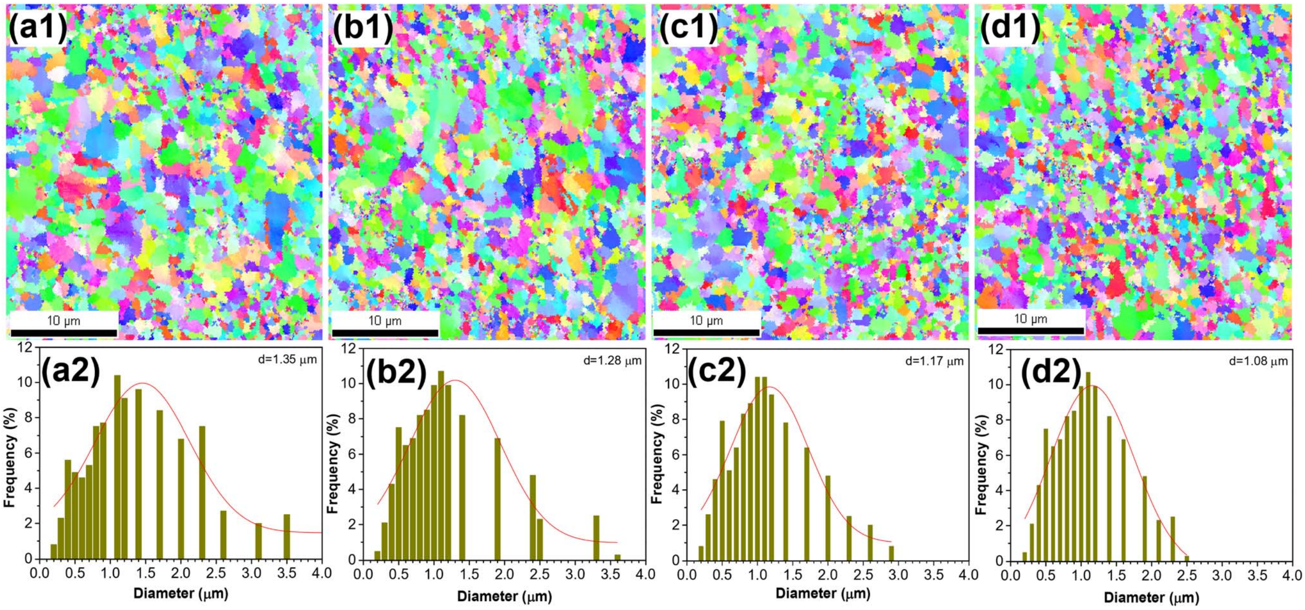

Fig. 4 EBSD inverse pole figure (IPF) map and grain size distribution of (a1 and a2) S0, (b1 and b2) S1, (c1 and c2) S2 and (d1 and d2) S3.

3.4. Wear properties

Fig. 7a presents the COF of SiC@CNT NW/Cu composites, showing that pure Cu exhibits the highest value, whereas incorporating SiC@CNT NWs into the Cu matrix markedly reduces the COF. The high COF of pure Cu can be attributed to its work-hardening behavior and strong adhesion between the frictional surfaces. As the SiC@CNT NW content increases, the COF curves exhibit a downward trend, with lower fluctuations observed for the composites. The reduction in COF is primarily due to the solid-lubricant effect of SiC@CNT NWs, which hinders direct contact between the sliding surfaces. The fluctuations are likely caused by the non-uniform distribution of SiC@CNT NWs over certain regions of the composite surface. The average COF values for S0, S1, S2, and S3 are 0.55, 0.44, 0.36, and 0.33, respectively. At a SiC@CNT NW content of 3 vol%, the COF reaches a minimum of about 0.33—approximately 40% lower than that of pure Cu. Similar to other composites containing solid lubricants, this significant reduction is linked to a substantial increase in the lubricating film coverage on the contact surface, which in this case depends on the content and dispersion of SiC@CNT NWs.

Fig. 7b shows the specific wear rate of the prepared samples. Specific wear rate was found to be 4.54×10^{-6}, 3.85×10^{-6}, 2.98×10^{-6} and 2.11×10^{-6} mm^3 N^{-1} m^{-1} for the composite S0, S1, S2 and S3, respectively. As a result, the specific wear rate of the composite S1, S2 and S3 is reduced by about 15%, 34% and 53% compared to the S0. Pure Cu shows large fluctuations in COF and wear rate during testing, primarily due to its high ductility, which enables energy absorption through plastic deformation and delays crack initiation on the frictional or subsurface regions.[6,25] In comparison, the consistent decrease in wear rate with increasing SiC@CNT NW content indicates that higher reinforcement levels yield smoother surfaces and improved wear resistance, confirming the effectiveness of SiC@CNT NWs in enhancing composite performance. In addition to enhancing

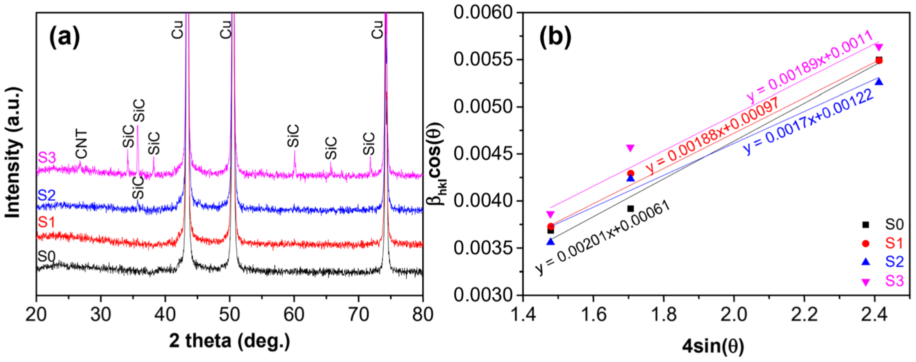

Fig. 5 (a) XRD patterns of prepared composites (S0, S1, S2, S3) and (b) the relationship between $\beta \cos \theta$ and $\sin \theta$ calculated by the William–Hall method.

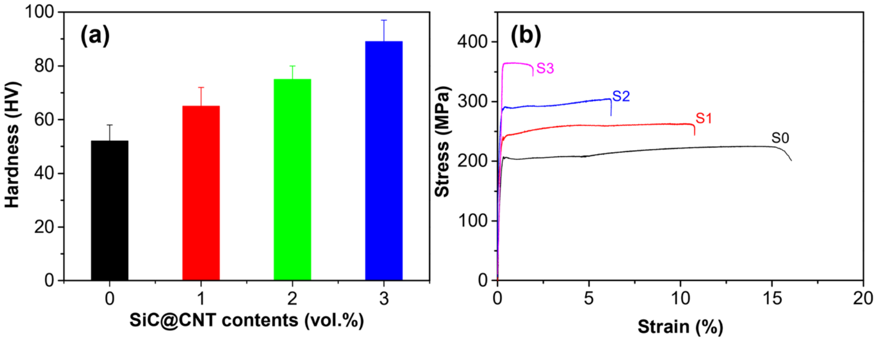

Fig. 6 (a) Hardness and (b) stress–strain curves of S0, S1, S2 and S3.

the hardness and strength of the composite, this also contributes to reducing the friction coefficient and specific wear rate.

To elucidate the wear mechanisms, the worn surface microstructures were examined. Fig. 8 presents optical images of the wear tracks for the prepared samples. The wear track of pure Cu (S0) shows a greater width and depth compared to the composites. With increasing SiC@CNT NW content, the wear track size decreases and the surface becomes smoother, consistent with the COF and wear rate trends discussed earlier. SEM observations reveal that S0 exhibits a severely rough surface, characterized by continuous grooves, numerous craters, and delamination, indicating substantial material removal and pull-out during plastic deformation (Fig. 9a and b). Friction during tribological testing likely generated high contact temperatures, promoting oxidation of the worn surfaces, as confirmed by EDS spectra and mapping (Fig. 10a and a1–a4). The detection of Cu and O elements suggests the formation of oxide phases, which can hinder dislocation motion at the interface, causing stress and strain concentration in the subsurface. When the local stress exceeds the rupture strength, cracks form, leading to significant wear loss. Fig. 9c and d show the worn surface of composite S3, where mainly continuous grooves and minimal delamination are observed. Abrasive debris particles are also present, while the absence of craters indicates a significant improvement in wear resistance compared to S0. This suggests that the dominant wear mechanism for S3 is abrasive wear. With increasing SiC@CNT NW content, the COF decreases, resulting in lower contact temperatures during sliding. Consequently, oxide formation is reduced, allowing greater plastic deformation before surface rupture. This leads to a lower wear rate and smoother surfaces at higher reinforcement levels. EDS analysis (Fig. 10b and b1–b4) confirms the presence of O, Si, and C on the worn surface, suggesting that SiC@CNT NWs are extruded from the composite and distributed across the contact surface. This distribution not only inhibits oxidation of the Cu matrix but also reduces friction due to the low shear strength of SiC@CNT NWs. When the SiC@CNT NWs are discontinuous, they are quickly removed by friction, explaining the minimal COF reduction at low reinforcement levels. In contrast, higher SiC@CNT NW content promotes the formation of continuous films along the wear track, substantially reducing both friction and wear rate.

3.5. Electrical and thermal properties

The influence of SiC@CNT NW content on the electrical and thermal conductivities is presented in Fig. 11. The results show that increasing the amount of reinforcement leads to a decrease in both electrical and thermal conductivities compared with pure Cu fabricated under the same conditions. The reduction in electrical conductivity may be attributed to enhanced electron scattering at the interfaces between SiC@CNT NWs and the Cu matrix. As the reinforcement content increases, the number of SiC@CNT–Cu interfacial regions also increase, thereby raising

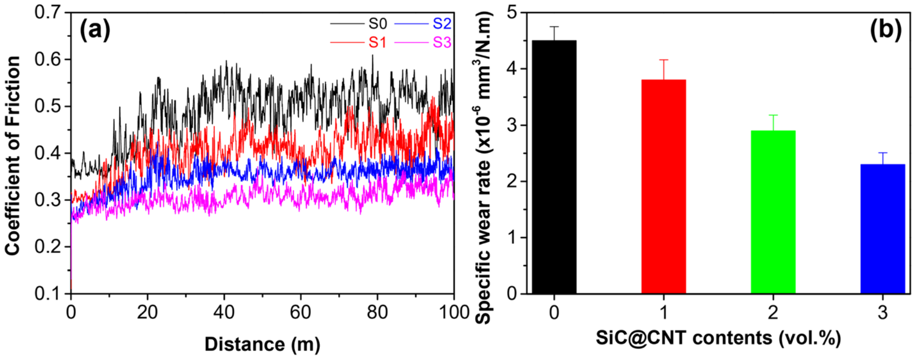

Fig. 7 (a) Friction coefficient and (b) specific wear rate of prepared samples.

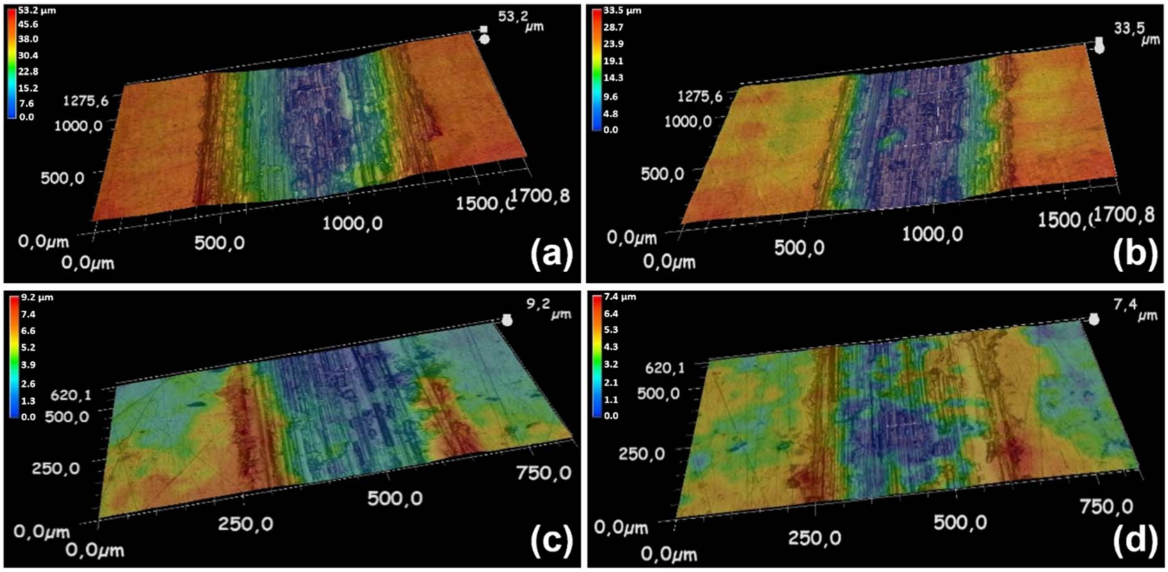

Fig. 8 Optical images of wear tracks of (a) S0, (b) S1, (c) S2 and (d) S3.

the overall electrical resistivity. In addition, the intrinsically low electrical of SiC may further contribute to the deterioration of these properties in the composites. The decrease in thermal conductivity of the composites can be explained by the formation of interfacial thermal barriers between the embedded SiC@CNTs and the Cu matrix, which impede heat transfer. The reduced thermal conductivity can also result from the defect formation on the CNT surfaces during the milling, surface functionalization, and SiC phase transformation processes. These defects induce significant phonon scattering, thus reducing heat transport efficiency.

Fig. 12a shows the relative expansion ($\Delta L/L_0$) of SiC@CNT NW/Cu composites with varying reinforcement contents. The $\Delta L/L_0$ decreases as the SiC@CNT NW fraction increases, leading to corresponding CTE values of 15.6×10^{-6}, 14.7×10^{-6}, 14.1×10^{-6}, and 13.5×10^{-6} K^{-1} for S0, S1, S2, and S3, respectively. This reduction could be attributed to the inherently lower CTE of SiC@CNT NWs compared to the Cu matrix. In addition,

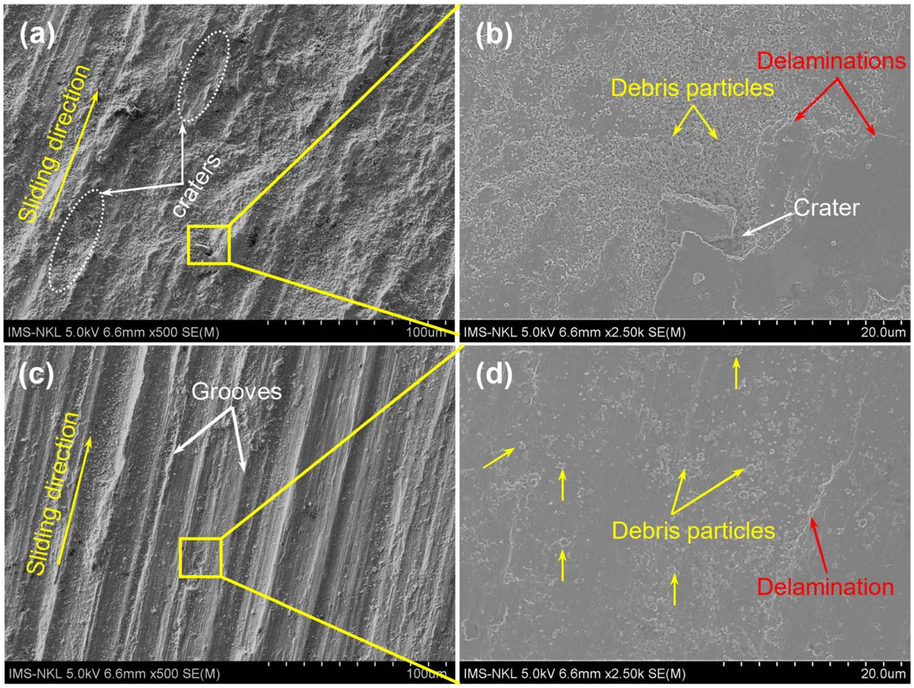

Fig. 9 SEM images of wear tracks of (a and b) S0 and (c and d) composite S3.

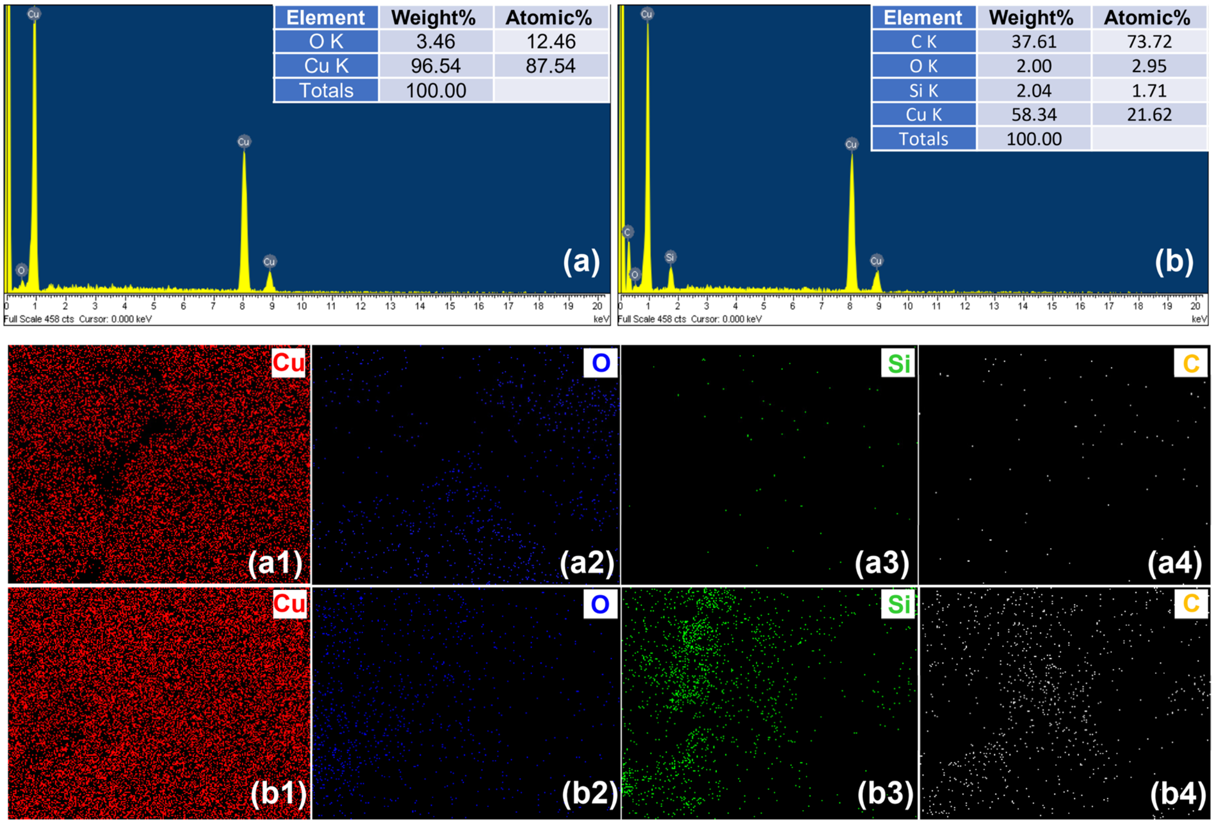

Element	Weight%	Atomic%
O K	3.46	12.46
Cu K	96.54	87.54
Totals	100.00	

Element	Weight%	Atomic%
C K	37.61	73.72
O K	2.00	2.95
Si K	2.04	1.71
Cu K	58.34	21.62
Totals	100.00	

Fig. 10 EDS spectra and mappings of wear tracks of (a and a1–a4) S0 and (b and b1–b4) S3.

residual stresses induced by the thermal expansion mismatch between the Cu matrix and the reinforcement significantly affect thermal expansion behavior.[55,56] The mismatch creates a residual stress field in which pores experience compressive stress, reducing pore volume. Consequently, higher porosity corresponds to lower thermal expansion and CTE, and *vice versa*.[55] To quantify the effect of SiC content on the composite CTE, an efficiency factor (F) is calculated as defined in eqn (4):[57]

$$F = \frac{\alpha_c - \alpha_m}{V_f} \tag{4}$$

where α_c and α_m are the CTE values of the composite and Cu, respectively; V_f is the SiC@CNT NWs volume percentage. The F values were calculated to be 90, 75 and 70 for composite S1, S2 and S3, respectively. Thus, the F values decrease with increasing SiC@CNT NW contents in the composites. This result is consistent with the relative density of the composites as discussed in the previous section.

To evaluate the influence of the SiC@CNT NWs reinforcement on the CTE of the composites, several theoretical models were employed to calculate the composite's CTE, including the Rule of Mixtures (ROM) (eqn (5)) and Turner's model (eqn (6)):

$$\alpha_c = \alpha_{Cu}V_{Cu} + \alpha_f V_f \tag{5}$$

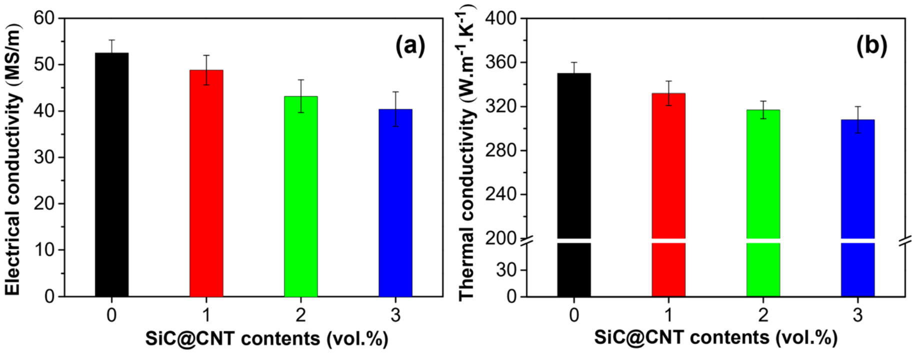

Fig. 11 (a) Electrical conductivity and (b) thermal conductivity of the prepared composites.

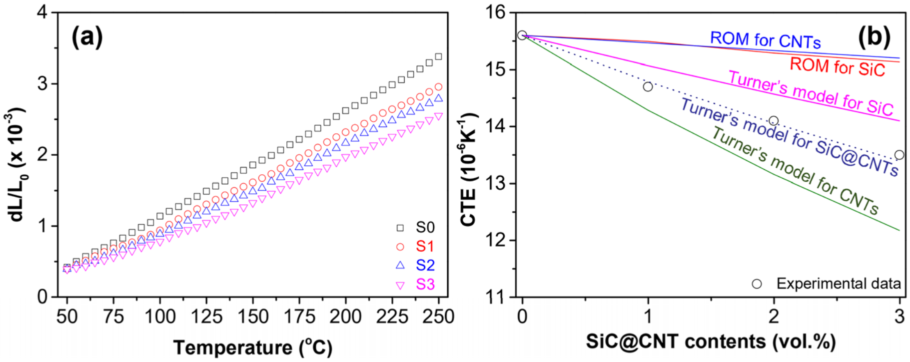

Fig. 12 (a) Thermal expansion and (b) calculated CTE of prepared samples using different theoretical models.

$$\alpha_c = \frac{\alpha_{Cu} V_{Cu} E_{Cu} + \alpha_f V_f E_f}{V_{Cu} E_{Cu} + V_f E_f} \tag{6}$$

where α is the CTE, V_f is the volume fraction of the reinforcement, and E is the elastic modulus. The subscripts c, Cu, and f refer to composite, Cu matrix and reinforcement materials, respectively. Since the theoretical α and E of SiC@CNT NWs have not been specifically determined, the theoretical α and E values of the individual reinforcement materials, namely CNTs ($\alpha = 0$,[58] $E = 1000$ GPa (ref. 59)) and SiC ($\alpha = 2.4 \times 10^{-6}\ \mathrm{K}^{-1}$,[60] $E = 450$ GPa (ref. 61)), were considered and used in the calculations. Fig. 12b presents a comparison between the values calculated using theoretical models and the corresponding experimental results. The obtained results indicate that the CTE values predicted by the ROM model are significantly higher than the experimental data. This discrepancy is attributed to the fact that the ROM model does not account for the influence of the E of both the Cu matrix and the reinforcement phase. In contrast, the Turner model incorporates the E of the reinforcement material. The results indicated that the α values of the composites calculated using the Turner model align well with the experimental trends. It is interesting to note that the α values predicted using the theoretical properties of SiC are higher than the experimental values, whereas those calculated using the CNT parameters are lower than the experimental data. This observation suggests that the actual α and E of SiC@CNT NWs differ substantially from those of SiC and CNTs. By approximating the theoretical results obtained from Turner's model with different assumed parameters, the best fitting values α and E of SiC@CNT NWs were determined to be $1.8 \times 10^{-6}\ \mathrm{K}^{-1}$ and 680 GPa, respectively. Consequently, the CTE of SiC@CNT NWs is found to be higher than that of CNTs but lower than that of SiC.

4. Conclusions

SiC@CNT nanowire-reinforced Cu composites were successfully fabricated *via* the powder metallurgy route. The SiC@CNT nanowires, with diameters ranging from 100 to 200 nm, were dispersed in Cu powder through a combination of tip-sonication and freeze-drying processes. The resulting composites exhibited a relative density exceeding 98%. Incorporation of SiC@CNT nanowires led to substantial enhancements in mechanical performance, with hardness and ultimate tensile strength increasing by up to 71% and 64%, respectively, compared with pure Cu. Moreover, increasing nanowire content progressively reduced both the friction coefficient and specific wear rate, owing to the synergistic effects of the self-lubricating nature of SiC@CNT nanowires and the improved mechanical strength. The CTE of the composites also decreased with higher nanowire loading, which is attributed to the intrinsically lower CTE of SiC@CNT nanowires relative to the Cu matrix.

Conflicts of interest

The authors declare no possible conflict of interests.

Data availability

The authors confirm that the data supporting the findings of this study are available within the articles. Raw data that support the findings of this study are available from the corresponding author, upon reasonable request.

Acknowledgements

This work was financially supported by the Institute of Materials Science, Vietnam Academy of Science and Technology under project CSCL.04.03/24-25.

References

1 F. Ogawa and C. Masuda, *Mater. Sci. Eng., A*, 2021, **820**, 141542.
2 Z. Zhong, X. Jiang, H. Sun, Z. Wu, L. Yang and A. Matamoros-Veloza, *Adv. Eng. Mater.*, 2024, **26**, 2401392.
3 K. Pooja, N. Tarannum and P. Chaudhary, *Discover Mater.*, 2025, **5**, 1–45.
4 W. Li, D. Li, Q. Fu and C. Pan, *RSC Adv.*, 2015, **5**, 80428–80433.
5 L. Wang, Y. Cui, S. Yang, B. Li, Y. Liu, P. Dong, J. Bellah, G. Fan, R. Vajtai and W. Fei, *RSC Adv.*, 2015, **5**, 19321–19328.
6 M. Wu, Z. Chen, C. Huang, K. Huang, K. Jiang and J. Liu, *RSC Adv.*, 2019, **9**, 39883–39892.

7 M. R. Akbarpour, F. Gazani, H. Mousa Mirabad, I. Khezri, A. Moeini, N. Sohrabi and H. S. Kim, *Prog. Mater. Sci.*, 2023, **140**, 101191.

8 N. M. Tuan, N. Van Toan, L. Van Duong, V. T. Long, T. B. Trung, P. Van Trinh and D. D. Phuong, *IEEE Access*, 2024, **12**, 7853–7863.

9 L. Van Duong, N. N. Anh, T. B. Trung, L. D. Chung, N. Q. Huan, D. T. Nhung, M. T. Phuong, P. N. Minh, D. D. Phuong and P. Van Trinh, *Diamond Relat. Mater.*, 2020, **108**, 107980.

10 K. Singh, V. Khanna, Sonu, S. Singh, S. A. Bansal, V. Chaudhary and A. Khosla, *J. Mater. Res. Technol.*, 2023, **24**, 8572–8605.

11 V. Kumar, A. Singh, Ankit and G. Gautam, *Interactions*, 2024, **245**, 357.

12 Y. F. Yan, S. Q. Kou, H. Y. Yang, S. L. Shu, F. Qiu, Q. C. Jiang and L. C. Zhang, *Int. J. Extreme Manuf.*, 2023, **5**, 032006.

13 A. S. Prosviryakov, *J. Alloys Compd.*, 2015, **632**, 707–710.

14 D. Zhang, H. Guli, J. Luo, C. Wu and J. Wang, *J. Wuhan Univ. Technol., Mater. Sci. Ed.*, 2018, **33**, 43–48.

15 D. D. Zhang, X. Y. He, H. Zhao and Y. L. Gao, *Mater. Sci. Technol.*, 2022, **38**, 5–11.

16 Y. Chen, R. Ud-din, T. Yang, T. Li, C. Li, A. Chu and Y. Zhao, *Materials*, 2023, **16**, 4819.

17 S. F. Moustafa, Z. Abdel-Hamid and A. M. Abd-Elhay, *Mater. Lett.*, 2002, **53**, 244–249.

18 H. Lin, X. Guo, K. Song, J. Feng, S. Li and X. Zhang, *Nanotechnol. Rev.*, 2021, **10**, 62–72.

19 M. R. Akbarpour, H. Mousa Mirabad and S. Alipour, *Ceram. Int.*, 2019, **45**, 3276–3283.

20 M. R. Akbarpour, F. Gazani, H. Mousa Mirabad, I. Khezri, A. Moeini, N. Sohrabi and H. S. Kim, *Prog. Mater. Sci.*, 2023, **140**, 101191.

21 N. T. Câmara, R. A. Raimundo, C. S. Lourenço, L. M. F. Morais, D. D. S. Silva, R. M. Gomes, M. A. Morales, D. A. Macedo, U. U. Gomes and F. A. Costa, *Adv. Powder Technol.*, 2021, **32**, 2950–2961.

22 G. Celebi Efe, T. Yener, I. Altinsoy, M. Ipek, S. Zeytin and C. Bindal, *J. Alloys Compd.*, 2011, **509**, 6036–6042.

23 M. R. Akbarpour, E. Salahi, F. Alikhani Hesari, A. Simchi and H. S. Kim, *Mater. Sci. Eng., A*, 2013, **572**, 83–90.

24 M. R. Akbarpour, E. Salahi, F. Alikhani Hesari, H. S. Kim and A. Simchi, *Mater. Des.*, 2013, **52**, 881–887.

25 M. R. Akbarpour, H. Mousa Mirabad and S. Alipour, *Ceram. Int.*, 2019, **45**, 3276–3283.

26 M. R. Akbarpour, E. Salahi, F. Alikhani Hesari, A. Simchi and H. S. Kim, *Ceram. Int.*, 2014, **40**, 951–960.

27 S. C. Tjong and K. C. Lau, *Mater. Lett.*, 2000, **43**, 274–280.

28 G. Chen, S. Guo, H. Zhang, H. Xiong and L. Gan, *Mater. Today Commun.*, 2022, **31**, 103233.

29 S. C. Yoo, D. Lee, S. W. Ryu, B. Kang, H. J. Ryu and S. H. Hong, *Prog. Mater. Sci.*, 2023, **132**, 101034.

30 R. M. Sundaram, A. Sekiguchi, M. Sekiya, T. Yamada and K. Hata, *R. Soc. Open Sci.*, 2018, **5**(11), 180814.

31 X. Ren, Y. Chang and C. Ge, *Int. J. Mol. Sci.*, 2024, **25**, 12957.

32 Z. Wang, X. Zu, F. Gao and W. J. Weber, *Phys. Rev. B: Condens. Matter Mater. Phys.*, 2008, **77**, 224113.

33 G. Cheng, T. H. Chang, Q. Qin, H. Huang and Y. Zhu, *Nano Lett.*, 2014, **14**, 754–758.

34 H. K. Seong, H. J. Choi, S. K. Lee, J. Il Lee and D. J. Choi, *Appl. Phys. Lett.*, 2004, **85**, 1256–1258.

35 P. Hu, S. Dong, X. Zhang, K. Gui, G. Chen and Z. Hu, *Sci. Rep.*, 2017, **7**, 1–10.

36 L. Zhang, S. Yang, M. Xiao, L. Chen, J. Sun, J. Ding, X. Li, Y. Gong, K. Zheng, X. Zhang and X. Tian, *Ceram. Int.*, 2022, **48**, 25382–25389.

37 S. Gu, H. Yu, X. Wu, J. Wang, B. Fu, X. Lu, J. Li, L. Wang and W. Jiang, *J. Eur. Ceram. Soc.*, 2025, **45**, 117603.

38 Y. Qin, B. Wang, X. Hou, L. Li, C. Guan, Z. Pan, M. Li, Y. Du, Y. Lu, X. Wei, S. Xiong, G. Song, C. Xue, W. Dai, C. Te Lin, J. Yi, N. Jiang and J. Yu, *Compos. Commun.*, 2022, **29**, 101008.

39 Y. Yao, X. Zeng, G. Pan, J. Sun, J. Hu, Y. Huang, R. Sun, J. Bin Xu and C. P. Wong, *ACS Appl. Mater. Interfaces*, 2016, **8**, 31248–31255.

40 Y. Huang, J. Hu, Y. Yao, X. Zeng, J. Sun, G. Pan, R. Sun, J. Bin Xu and C. P. Wong, *Adv. Mater. Interfaces*, 2017, **4**, 1700446.

41 S. C. Yoo, B. Kang, P. Van Trinh, D. D. Phuong and S. H. Hong, *Sci. Rep.*, 2020, **10**, 1–11.

42 H. Liu, X. Zhang, K. Li, Q. Cui, L. Han, Q. Shen, H. Li and X. Yin, *Carbon*, 2024, **228**, 119411.

43 H. Mei, W. Yang, X. Zhao, L. Yao, Y. Yao, C. Chen and L. Cheng, *Mater. Des.*, 2021, **197**, 109271.

44 A. V. Zavorin, V. L. Kuznetsov, S. I. Moseenkov, A. G. Selyutin, A. V. Ishchenko and T. O. Tsendsuren, *Diamond Relat. Mater.*, 2023, **137**, 110113.

45 P. Van Trinh, N. N. Anh, N. T. Tam, N. T. Hong, P. N. Hong, P. N. Minh and B. H. Thang, *RSC Adv.*, 2017, **7**, 49937–49946.

46 A. Kasperski, A. Weibel, C. Estournès, C. Laurent and A. Peigney, *Carbon*, 2013, **53**, 62–72.

47 C. Guiderdoni, E. Pavlenko, V. Turq, A. Weibel, P. Puech, C. Estournès, A. Peigney, W. Bacsa and C. Laurent, *Carbon*, 2013, **58**, 185–197.

48 C. Guiderdoni, C. Estournès, A. Peigney, A. Weibel, V. Turq and C. Laurent, *Carbon*, 2011, **49**, 4535–4543.

49 X. Zhang, S. Li, B. Pan, D. Pan, L. Liu, X. Hou, M. Chu, K. Kondoh and M. Zhao, *Carbon*, 2019, **155**, 686–696.

50 A. Khorsand Zak, W. H. Abd. Majid, M. E. Abrishami and R. Yousefi, *Solid State Sci.*, 2011, **13**, 251–256.

51 F. W. Gayle and F. S. Biancaniello, *Nanostruct. Mater.*, 1995, **6**, 429–432.

52 O. S. Fatoba, O. Popoola and A. P. I. Popoola, *Silicon*, 2015, **7**, 351–356.

53 S. Nosewicz, P. Bazarnik, M. Clozel, Ł. Kurpaska, P. Jenczyk, D. Jarząbek, M. Chmielewski, B. Romelczyk-Baishya, M. Lewandowska, Z. Pakieła, Y. Huang and T. G. Langdon, *Arch. Civ. Mech. Eng.*, 2021, **21**, 1–19.

54 L. Han, J. Wang, S. Guo, Y. Chen, C. Shi, Y. Huang, Z. Wang, Y. Liu and N. Zhao, *Mater. Des.*, 2022, **220**, 110869.

55 E. B. Moustafa and M. A. Taha, *Int. J. Miner., Metall. Mater.*, 2021, **28**, 475–486.

56 Z. Lei, K. Zhao, Y. Wang and L. An, *J. Mater. Sci. Technol.*, 2014, **30**, 61–64.

57 W. S. AbuShanab, E. B. Moustafa, E. Ghandourah and M. A. Taha, *Results Phys.*, 2020, **19**, 103343.

58 Y. Yosida, *J. Appl. Phys.*, 2000, **87**, 3338–3341.
59 Y. Zare and K. Y. Rhee, *J. Mater. Res. Technol.*, 2020, **9**, 22–32.
60 N. M. Sultan, T. M. B. Albarody, H. K. M. Al-Jothery, M. A. Abdullah, H. G. Mohammed and K. O. Obodo, *Materials*, 2022, **15**, 6229.
61 A. H. Gomes de Mesquita, *Acta Crystallogr.*, 1967, **23**, 610–617.